

MID-INFRARED SPECTROPHOTOMETRIC OBSERVATIONS OF FRAGMENTS B AND C OF COMET 73P/SCHWASSMANN-WACHMANN 3

DAVID E. HARKER¹, CHARLES E. WOODWARD²,
MICHAEL S. KELLEY³, MICHAEL L. SITKO⁴, DIANE H. WOODEN⁵,
DAVID K. LYNCH⁶, RAY W. RUSSELL⁷,

ABSTRACT

We present mid-infrared spectra and images from the GEMINI-N (+Michelle) observations of fragments SW3-[B] and SW3-[C] of the ecliptic (Jupiter Family) comet 73P/Schwassmann-Wachmann 3 pre-perihelion. We observed fragment B soon after an outburst event (between 2006 April 16 – 26 UT) and detected crystalline silicates. The mineralogy of both fragments was dominated by amorphous carbon and amorphous pyroxene. The grain size distribution (assuming a Hanner modified power-law) for fragment SW3-[B] has a peak grain radius of $a_p \sim 0.5 \mu\text{m}$, and for fragment SW3-[C], $a_p \sim 0.3 \mu\text{m}$; both values larger than the peak grain radius of the size distribution for the dust ejected from ecliptic comet 9P/Tempel 1 during the Deep Impact event ($a_p = 0.2 \mu\text{m}$). The silicate-to-carbon ratio and the silicate crystalline mass fraction for the submicron to micron-size portion of the grain size distribution on the nucleus of fragment SW3-[B] was $1.341^{+0.250}_{-0.253}$ and $0.335^{+0.089}_{-0.112}$, respectively, while on the nucleus of fragment SW3-[C] was $0.671^{+0.076}_{-0.076}$ and $0.257^{+0.039}_{-0.043}$, respectively. The similarity in mineralogy

¹Center for Astrophysics and Space Sciences, University of California, San Diego, 9500 Gilman Drive, La Jolla, CA 92093-0424, *dharker@ucsd.edu*

²Department of Astronomy, School of Physics and Astronomy, 116 Church Street, S. E., University of Minnesota, Minneapolis, MN 55455, *chelsea@astro.umn.edu*

³The University of Maryland, Dept. of Astronomy, College Park, MD 20742-2421

⁴Space Science Institute, Boulder, CO 80301

⁵NASA Ames Research Center, Space Science Division, MS 245-1, Moffett Field, CA 94035-1000, *diane.h.wooden@nasa.gov*

⁶Thule Scientific, P.O. Box 953, Topanga, CA 90290

⁷The Aerospace Corporation, Los Angeles, CA 90009

and grain properties between the two fragments implies that 73P/Schwassmann-Wachmann 3 is homogeneous in composition. The slight differences in grain size distribution and silicate-to-carbon ratio between the two fragments likely arises because SW3-[B] was actively fragmenting throughout its passage while the activity in SW3-[C] was primarily driven by jets. The lack of diverse mineralogy in the fragments SW3-[B] and SW3-[C] of 73P/Schwassmann-Wachmann 3 along with the relatively larger peak in the coma grain size distribution suggests the parent body of this comet may have formed in a region of the solar nebula with different environmental properties than the natal sites where comet C/1995 O1 (Hale-Bopp) and 9P/Tempel 1 nuclei aggregated.

Subject headings: comets: general: comets: individual (73P/Schwassmann-Wachmann 3)
:dust: modeling

1. INTRODUCTION

Comet nuclei contain some of the least thermally- and least aqueously-altered materials extant in the solar system and are highly porous agglomerates of ice and dust grains, perhaps with highly stratified, inhomogeneous layers of varied density, porosity, and composition (Harker et al. 2007; Belton et al. 2006) formed by layered accretion of icy planetesimals. The latter may or may not have aggregated from specific radial zones in the protoplanetary disk to form the nascent nuclei of comets, ultimately giving rise to the two comet families, ecliptic comets (ECs; including Jupiter Family comets and active Centaurs) and nearly isotropic comets (NICs; including long-period Oort cloud and Halley-type comets).

Recent dynamical models by the ‘Nice group’ indicate that Jupiter ejected bodies from the solar system’s gravitational potential and into the Oort Cloud to become NICs. Comet nuclei that formed in the trans-Neptune region, *in situ* in the Kuiper Belt (KB), and the possible few ejected by Jupiter into the KB, survived dynamically to become ECs (Morbidelli et al. 2004; Whitman et al. 2006). As collisions are frequent in the Kuiper Belt (Pan et al. 2005), Jupiter-family comets (ECs) could be chips off of larger Kuiper Belt Objects (KBOs). Therefore, the structure of EC nuclei may be very different from NICs. On the other hand, Oort cloud (NIC) comets (i.e., long-period) were gravitationally scattered to the Oort cloud (Öört 1951) where they suffered no further collisions (Stern 2003). Once perturbed into the inner solar system, NICs have short life times compared to EC comets (A’Hearn et al. 1985). ECs have notably less activity than NICs (A’Hearn et al. 1985; Meech & Svoren 2004). Lower activity and lower dust production rates result in less thermal dust emission making dust properties of ECs relatively unknown compared to brighter NICs (Wooden et al. 2007; Sitko et al.

2004; Hanner, Lynch, & Russell 1994).

The strongest tests for new dynamical models of solar system formation processes are the compositions of comets, and in particular, the diversity of the gas-to-dust ratio and dust composition within any given comet’s coma coupled with variations in the latter physical characteristics (among others) between comets within a dynamical family and between dynamical families. Notably, solar nebula models for thermal processing and radial transport (Boss 2004; Cuzzi et al. 1993) of grains are constrained by the crystalline silicate mass fraction deduced for comets (Wooden et al. 2007; Wooden 2005), as well as the (controversial) presence of aqueous altered grain components. Amorphous silicates in comets are thought to be presolar ISM silicate grains (Wooden 2002; Hanner & Bradely 2004) because of their high abundance in the ISM (Li & Draine 2001) and ubiquitous presence as glassy spherules (GEMS) in cometary interplanetary dust particles (Bradley 1994; Bradley et al. 1999; Hanner & Bradely 2004). On the other hand, crystalline silicates are relatively rare ($\lesssim 2.2 - 5\%$) in the ISM (Kemper et al. 2004, 2005; Li & Draine 2001) yet are abundant in many comets. Crystalline silicates in comets are either high-temperature (≈ 1450 K) condensates (Grossman 1972), or amorphous silicates annealed into crystals at ~ 1000 K (Hallenbeck et al. 1998; Wooden 2005; Wooden et al. 2007) in the inner zones of the early ($\lesssim 0.3$ Myr-old) solar nebula (Bockelée-Morvan et al. 2002), or annealed in nebular shocks at 5-10 AU ($\lesssim 1$ Myr-old) (Harker & Desch 2002). In models of turbulent mixing, the early formation of crystals in the hot inner zones of the solar nebula are concurrent with rapid disk spreading (0.3 Myr) suggests a uniform crystalline-to-amorphous silicate ratio between comets (Bockelée-Morvan et al. 2002). In contrast, viscous dissipation models may yield a radial gradient in the crystalline silicate mass fraction that spreads to only 20 AU in 1 Myr (Wooden et al. 2007; Ciesla 2007), making it harder to explain crystals in comets that formed in the trans-Neptune zone. Strong constraints for nebula models include the high crystalline silicate mass fraction ($\sim 25\% - 50\%$) deduced from modeling NIC C/1995 O1 (Hale-Bopp) (Harker et al. 2004), NIC C/2001 Q4 (NEAT) (Harker et al. 2005; Wooden et al. 2004), the ejecta from the EC 9P/Tempel 1 during *Deep Impact* (Harker et al. 2005, 2007), and the EC 78P/Gehrels 2 (Watanabe et al. 2005). *Stardust* samples from EC 81P/Wild 2 contain abundant crystalline silicates (Ebel et al. 2006) and even higher temperature calcium-aluminum inclusion (CAI)-type minerals. In contrast, other ECs have a low ($\ll 50\%$) crystalline silicate mass fractions: pre-impact 9P/Tempel 1 (Lisse et al. 2006), 103P/Hartley 2 (Crovisier et al. 2000; Crovisier 1999), and 29P/Schwassmann-Wachmann 1 (Stansberry et al. 2004). Thus, assessing the composition of cometary nuclei is critical to understanding the origins of comets (Ehrenfreund et al. 2004; Hanner & Bradely 2004; Crovisier 2007) and the formation of the solar system.

Contrasts between EC and NIC family grain properties often rely on comparisons be-

tween ground-based remote-sensing studies and the *in situ* sampling of coma dust in comets such as 1P/Halley, 81P/Wild 2 or the 9P/Tempel 1 (henceforth 9P) Deep Impact ejecta analysis. Frequently, the 10 μm spectra of short-period ECs exhibit a broad and weak 10 μm feature, of order 10-20% above the 8 to 13 μm blackbody continuum (Hanner & Zolensky 2010) and little evidence for the presence of crystalline silicates – a result of space weathering, thermal processing, and de-volatilization arising from frequent perihelion passage, whereas in NIC comets such emission is common (Kelley & Wooden 2009). Surprisingly, the Deep Impact event excavated sub-surface materials containing a significant population of small grains, including crystalline silicate species, unlike the grain population dominant in the quiescent coma of the EC 9P. The observed 10 and 20 μm spectra and composite thermal spectral energy distribution (SED) models of the 9P dust ejecta were similar in characteristics to those deduced for the coma grains in comet C/1995 O1 (Hale-Bopp), a NIC. Harker et al. (2007), Sugita et al. (2005), and Lisse et al. (2006) among others conjectured that the interior of 9P may be comprised of less processed, more primitive, or pristine grain material. Therefore, inference between comet families drawn from the study of coma dust is a challenge. The assertion that ECs are compositionally distinct from NICs as a class is no longer valid based on the Deep Impact experiment (Hanner & Zolensky 2010).

In its 1995 apparition, the Jupiter-family comet 73P/Schwassmann-Wachmann 3 (henceforth SW3) exhibited a sudden increase in brightness (Crovisier et al. 2006) near perihelion breaking into three bright fragments and several fainter components (Scotii et al. 1996). The observing geometry of SW3’s next perihelion passage (orbital period $T = 5.36$ yr) was not very favorable for Earth-based observers (Sekanina 2005). During SW3’s 2006 return to perihelion ≈ 66 fragments were detected (Weaver et al. 2008), many of which were remnants of the splitting event of 1995 (Reach et al. 2009). Fragments SW3-[B] and [G] continued to split, and swarms of mini-comets were discovered in *Hubble Space Telescope* images of the tails of these fragments (Weaver et al. 2008). Fragmentation of this comet’s nucleus, a natural analogy to the Deep Impact mission, provided a rare opportunity to observe potentially pristine material from the progenitor interior (Della Russo et al. 2007).

Here we present mid-infrared narrowband imagery and spectroscopy (§2) and coma dust mineralogy derived from thermal grain models (§ 3) of the two largest surviving fragments, SW3-[B] and SW3-[C] during the 2006 apparition, discussing comparison (§4) between grain properties of this comet (one of the most active known ECs) to the putatively more primitive dust populating the coma of NIC comets such as C/1995 O1 (Hale-Bopp). Our conclusions are summarized in §5.

2. OBSERVATIONS

Mid-infrared (IR) 10 μm spectra and 10 and 20 μm images of fragments SW3-[B] and SW3-[C] of comet SW3 pre-perihelion (perihelion 2006 June 08 UT) on 2006 April 29.5 UT (fragment SW3-[B]) and 2006 April 30.5 UT (fragment SW3-[C]) were obtained using the Michelle imaging spectrograph on the 8-m Fredrick C. Gillett telescope (Gemini-N) on Mauna Kea, Hawaii conducted under program GN-2006A-DD-1. In addition, we obtained 20 μm spectra of fragment SW3-[B]. The observational summary is shown in Table 1.

Michelle has several mid-IR broad and narrow band filters (Alistair et al. 1997). For our observations, we used two narrow band filters: 1) the Si-5 filter with a central wavelength of 11.6 μm and width of 9.5%; and 2) the Qa filter with a central wavelength of 18.1 μm and width of 10.7%. Common mid-IR observing techniques (e.g., Joyce 1992), chopping the secondary ($\pm 15''$ at a 45° angle in the NW-SE direction) and nodding the telescope ($\pm 15''$ in the NW-SE direction) to reduce the thermal noise from the background and avoid contamination from the coma extending to the south west for both comets, were utilized. The brightness of the coma in the NW-SE direction for both fragments drops to the value of the background at 11.2 μm ($40.12 \text{ mJy arcsec}^{-2}$) at $6''$ away from the centralized core. A final image is produced by subtracting the two nod pairs.

Michelle uses a grating to produce spectra with wavelength coverage of $\approx 7.8 - 13.2 \mu\text{m}$ and $\approx 17.0 - 21.0 \mu\text{m}$ within the 10 μm and 20 μm ground-based atmospheric windows, respectively. A $0.6''$ wide slit was used for all of our spectral observations, providing a resolution of $R \sim 200$ and $R \sim 110$ at 10 μm and 20 μm , respectively. We chopped on array at the maximum allowable chop throw of $15''$ along the slit direction, perpendicular to the dispersion axis of Michelle.

Extraction of the comet and standard star spectra from the two-dimensional images used common mid-IR data reduction techniques (Joyce 1992): 1) two nod pairs are subtracted to produce a background subtracted image which contains both a positive and negative spectrum; 2) two extractions (spatial dimension of $1.0''$ yielding an effective aperture diameter of $0.87''$) are made to produce each spectrum: one is the source spectrum, and the other is extracted $6''$ to the north of the source spectrum for the purpose of calculating the residual background; 3) all of the counts at each pixel (i.e., wavelength) inside the source aperture are summed; 4) the sky extraction is used to calculate a median residual background value and variance, which is used to calculate the photometric error for the object spectrum; and 5) the median sky value is subtracted from the object spectrum. Nominally, a residual sky spectrum to the south of the source spectrum is also used to calculate the background value and variance. However, in this case, for both fragments, there is emission from the extended coma in this southern direction. Therefore, we have relied only on the northern sky extraction.

Using this technique does not affect the overall value of the sky, but simply does not enable better constraint of the uncertainties in the sky variances. This uncertainty is reflected in the larger 1-sigma error in the final spectrum. We increased the signal-to-noise of the data with a 3-point statistically weighted average boxcar function. This operation decreased the spectral resolution to $R = 129$ at $10 \mu\text{m}$. The spectral resolution is sufficient to identify mineral resonances that may exist (Harker et al. 2002; Wooden et al. 1999). In 100.8 s of on-source integration time, a given flux point in the final spectra has a root-mean-square (RMS) error of $2.5 \times 10^{-19} \text{ W cm}^{-2} \mu\text{m}^{-1}$.

Cohen standards (Cohen et al. 1996) which provide superior IR spectrophotometric calibration, and ATRAN atmospheric models (Lord 1993) are used to flux calibrate the spectra and correct for atmospheric extinction. The object spectrum is multiplied by the Cohen stellar template, divided by the extracted instrument spectrum of the standard, and finally multiplied by the ratio of the atmospheric transmission spectra calculated for the airmass of the comet and standard star. Photometric standards were also used to assess the seeing and derive estimates of the point-spread function (PSF). The average PSF FWHM was $0.4''$ at $11.6 \mu\text{m}$ and $0.5''$ at $18.1 \mu\text{m}$.

Figure 1 shows the 11.6 and $18.1 \mu\text{m}$ images of fragments SW3-[B] and SW3-[C], respectively. The 3-sigma detection limit of the coma of SW3-[B] extends $\sim 15''$ from the central nucleus region towards the south western direction at a position angle (PA) $\simeq 205^\circ$ in both images. Notably, there is a region of enhanced flux (32% above the expected flux of a standard $1/\rho$ decline in coma surface brightness, where ρ is the projected distance from the nucleus) approximately $3''$ away from the centralized condensed region that is observed at both wavelengths. The coma of SW3-[C] is fairly condensed ($0.6''$ at $11.6 \mu\text{m}$), the 3-sigma detection limit of the coma extending only about $\sim 8''$ at $\text{PA} \simeq 219^\circ$. We note that more sensitive *Spitzer* MIPS24 observations of 73P, obtained less than a week after our Michelle observations (2006 May 4 – 5 UT), showed that the surface brightness of the coma of fragment SW3-[B] extended some $4'$ while that of SW3-[C] extended $\simeq 5'$ (Reach et al. 2009). Isophote-contour maps derived from our SW3-[C] image do not reveal any enhanced regions of flux density, in contrast to the surface brightness morphology evident in the coma of fragment SW3-[B].

Figure 2 shows the location and orientation of the $0.6''$ wide spectral slit during the observation of each fragment, the location and size of the extraction areas for the spectra, and the extracted spectra. The slits were centered on the peak of the azimuthally-averaged coma surface brightness profile, essentially coincident with the nucleus (unresolved at our platescale), and rotated to align along the direction of the extended coma. Individual spectra were extracted in $1.0''$ segments in the spatial direction for mineralogical and grain analysis

(§3).

The spectral extraction apertures centered on the nucleus contain both nuclear and coma fluxes. In order to study the coma dust properties, we need to properly assess the nuclear contribution to the flux. We can deconvolve the relative contribution of the nucleus flux to the coma by analyzing the high spatial resolution images at $11.6 \mu\text{m}$. We take the PSF of the standard star HD 127665 as the shape of the nuclear contribution to the images. We assume a standard $1/\rho$ coma surface brightness decline. We derive the azimuthally-averaged cumulative photometry versus increasing ρ , i.e., from the peak flux pixel, for the image and for the sum of a scaled PSF and the $1/\rho$ -coma. By χ^2 -fitting the shape of the azimuthally-averaged coma profile, we constrain the contribution of the PSF to the image. By putting a synthetic beam of $0.6'' \times 1.0''$ on this solution, the nucleus is found to contribute $1.4\% \pm 0.2\%$ of the measured flux in the centered slit at $11.6 \mu\text{m}$ to a confidence level of 99% for fragment SW3-[B]. Our calculated scaling factor corresponds to an effective radius of the nucleus of $0.2 \text{ km} \pm 0.05 \text{ km}$ for fragment SW3-[B], equal to the lower limit of the nucleus radius determined by Howell et al. (2007). The nucleus contribution is subtracted from the central extracted spectrum of fragment SW3-[B], so we only need to model the remaining coma grains. From the $11.6 \mu\text{m}$ image of fragment SW3-[C], we determine that the flux at the central region is produced solely from the surrounding coma, and that there is no contribution to the flux from the embedded nucleus (at the 99% confidence level). Therefore, we do not apply a correction to the spectrum for fragment SW3-[C].

3. MODEL OF THERMAL EMISSION FROM DUST GRAINS

The Harker et al. (2002) thermal emission dust code was used to model the observed dust grain emission in the coma of fragments SW3-[B] and SW3-[C]. The model assumes that an optically-thin collection of discrete (singular mineralogy) dust particles reside at the heliocentric (r_h) and geocentric (Δ) distance of the comet at the epoch of observations (Table 1). The $10 \mu\text{m}$ mineralogy used in the model is derived from laboratory studies of interplanetary dust particles (IDPs, Wooden et al. 2000), micrometeorites (Bradley et al. 1999), the NASA *Stardust* mission (Brownlee et al. 2006) and other remote sensing modeling efforts (e.g., Hanner, Lynch, & Russell 1994; Harker et al. 2002; Wooden et al. 2004). Our selection of basic dust grain components is consistent with the major mineral groups used by other modelers to generate synthetic SEDs arising from dust thermal emission in the $10 \mu\text{m}$ region (Min et al. 2005; Sugita et al. 2005; Lisse et al. 2006; Werner et al. 2006). Amorphous silicates with chemical composition (stiochiometry) similar to olivine ($\text{Mg}_y\text{Fe}_{(1-y)}\text{SiO}_4$) and pyroxene ($\text{Mg}_x\text{Fe}_{(1-x)}\text{SiO}_3$) with $x = y = 0.5$ (i.e., $\text{Mg}/(\text{Mg} + \text{Fe}) = 0.5$) repro-

duce the broad width of the 10 μm feature. Mg-rich orthopyroxene is detected through its 9.3 and 10.5 μm features (Wooden et al. 1999; Harker et al. 2002). Mg-rich crystalline olivine is uniquely identified through its distinct, relatively narrow 11.2 μm silicate feature (Hanner, Lynch, & Russell 1994). Mg-rich crystalline species are defined as grains with a stoichiometry of $0.9 \leq x \lesssim 1.0$ ($Mg/(Mg + Fe) = 0.9$) (Wooden 2008; Koike et al. 2003; Chihara et al. 2002).

Lastly, the presence of amorphous carbon grains in the coma is required in order to reproduce the underlying featureless emission (continuum) in the 8 – 13 μm wavelength region. Other species such as PAHs, hydrous silicates (clays) and iron sulfides (see Werner et al. 2006; Gehrz et al. 2007), cannot be uniquely identified from our SW3 spectra. Therefore, these latter species are not included our model.

The amorphous grains are assumed to be spherical (Mie Theory) and range in size from 0.1 – 100 μm . The indices of refraction used in Mie Theory to calculate the optical efficiencies of each amorphous silicate materials are from Dorschner et al. (1995) and the amorphous carbon is from Edoh (1983). The submicron sized crystalline olivine grains are modeled using a continuous distribution of ellipsoids (CDE) with one of the crystallographic axes elongated to a ratio of 10:1:1 to match the wavelength of the emission features with laboratory experiments (Fabian et al. 2001). The use of elongated grains is supported by polarization measurements of the diffuse interstellar medium which suggest the presence of elongated grains, and condensation experiments which show the formation of elongated forsterite (Mg-pure) crystals (Fabian et al. 2001). The radii of the crystalline olivine grains ranges from 0.1 – 1.0 μm ; larger crystals do not well match the shape of the observed resonances in comet Hale-Bopp (Min et al. 2005). The indices of refraction for the three crystallographic axes of the crystalline olivine between 3 and 250 μm are from Jäger et al. (1998). The non-oriented crystalline olivine indices ranging from 0.2 – 2 μm are from the Jena Laboratory Group¹. The short wavelength indices are appended to each long wavelength axes prior to the CDE calculations. Note that the radius of the crystals is an “effective” radius, or the radius a crystal would be if it were spherical.

The temperature of each grain is calculated using a thermal equilibration calculation. In the coma, the grains reach radiative equilibrium quickly (Wooden 1979) as they enter into the coma. The temperature of the crystalline olivine grains are calculated using the “hot crystal model” presented in Harker et al. (2002): the temperature of the crystalline olivine grains are increased by 1.9 times over those predicted from the optical constants in order to fit the *Infrared Space Observatory* (ISO) SEDs from comet C/1995 O1 (Hale-Bopp) at

¹<http://www.astro.uni-jena.de/Laboratory/Database/databases.html>

2.9 AU (Croviser et al. 1997). The temperature increase was required to match the relative emission peak strengths in the 10 and 20 μm regions, and may be caused by crystals being in contact with warm material, or the crystals themselves contain some Fe making them Mg-rich, but not Mg-pure. We retain this “hot crystal model” in all of our comet modeling to compare results between comets, although the model awaits further constraining with additional long wavelength data from the comets observed by *Spitzer* (Kelley et al. 2006). An effect of using warm crystals in thermal models is the calculated dust species masses derived from mineral decomposition analysis are less than the mass fractions computed if cooler temperature grain populations were invoked. However, use of warm crystals does not affect the relative amount of crystalline silicates we calculate in the fragment comae of SW3.

For the grain size distribution, we use the Hanner modified power law (hereafter HGSD; Hanner, Lynch, & Russell 1994). In the HGSD, the relative number of each grain *size* is calculated by: $n(a) = (1 - a_o/a)^M (a_o/a)^N$, where a is the grain radius, $a_o = 0.1 \mu\text{m}$, the minimum grain radius, and M and N are independent parameters. Since N weights more of the larger radii particles and can be considered as the size distribution slope for large radii, it is best constrained at wavelengths longer than 13 μm . The value for N is set at three different values in the model: 1) $N = 3.4$ which weights more of the larger particles in the size distribution; 2) $N = 3.7$ is the canonical value we determined from our modeling of comet C/1995 O1 (Hale-Bopp) (Harker et al. 2002); and 3) $N = 4.2$ which weights more of the smaller particles in the size distribution. From the values of N and M , we also calculate the peak of the HGSD: $a_p = (M + N)/N$. The value a_p is not a freely varying parameter, but a calculated property of the size distribution. We varied M such that a_p changed by increments of 0.1 μm .

The amorphous dust can be modeled as porous grains (the crystals always remain solid). The fractal porosity of the amorphous grains is varied to create porous or “fluffy” particles (Lisse et al. 1998). The amount of vacuum is: $f = 1 - (a/a_o)^{(D-3)}$ with $D = 3.0$ corresponding to solid grains and $D = 2.5$ corresponding to the maximum fractal porosity allowed while still satisfying the assumptions of Mie Theory (Bazell & Dwek 1990).

Finally, the flux (in $\text{W cm}^{-2} \mu\text{m}^{-1}$) from each mineral is calculated by integrating over the grain size distribution between the minimum radius $a_o = 0.1 \mu\text{m}$ and the maximum grain radius $a_{max} = 100 \mu\text{m}$,

$$F_{em}(\lambda, r_h) = \frac{N_p}{\Delta^2} \int_{a_o}^{a_{max}} n(a) \pi a^2 Q_{em}(a, \lambda) B(\lambda, T_d(a)) da \quad (1)$$

where N_p is the number of particles at the peak of the grain size distribution if the peak of $n(a)$ is normalized to unity, Δ is the geocentric distance of the dust grain, $n(a) da$ is

the grain size distribution, $Q_{em}(a, \lambda)$ is the emission efficiency for a grain of radius $a(\mu\text{m})$ at wavelength $\lambda(\mu\text{m})$, and $T_d(\text{K})$ is the heliocentric distance dependent (r_h -dependent) dust temperature for a single grain size, a , calculated by radiative equilibrium. The flux from each mineral species is coadded and fit to the Gemini spectra by varying N_p . The best-fit is determined by calculating the lowest χ^2_ν (reduced χ^2) value at a confidence level of two-sigma.

4. RESULTS & DISCUSSION

4.1. Model Fits

The best-fit model parameters for SW3-[B] are listed in Table 2 and the spectral decomposition is shown in Fig. 3. Similarly, the best fit model parameters for SW3-[C] are listed in Table 3 and the spectral decomposition is shown in Fig. 4.

The grain properties of both SW3 fragments are similar. The grains range from being solid to moderately fractally porous ($D = 3.0 - 2.727$). Fractally porous coma grains in SW3 fragments are also required to explain the high fractional polarization measured in the optical I - and near-IR H -band at high phase angles and throughout the comae of SW3-[B] and SW3-[C] by Jones et al. (2008). The peak of the HGSD for fragment SW3-[B] in the anti-sunward direction is slightly larger ($\sim 0.5 \mu\text{m}$) than that of fragment SW3-[C] ($\sim 0.3 \mu\text{m}$). However, the grain population in SW3 overall is not dominated by extremely small particles as was evident in the comae C/1995 O1 (Hale-Bopp) or 9P post-Deep Impact (Wooden et al. 1999; Harker, Woodward, & Wooden 2005; Harker et al. 2007).

In both fragments, most of the thermal emission is dominated by amorphous (glassy) carbon and silicates. The silicate emission feature in both fragments is dominated by amorphous pyroxene grains, although there is some evidence for a population of amorphous olivine grains associated with the coma toward the nuclei of both fragments. Orthopyroxene is seen in the extended coma in both the sunward and anti-sunward direction of fragment SW3-[B], but only in the sunward direction, close to the nucleus ($1''$) in fragment SW3-[C]. A modest population of crystalline olivine grains is present in both fragments. The silicate crystalline mass fraction for the submicron to micron-size portion of the grain size distribution (Harker et al. 2002; Moreno et al. 2003), defined as $f_{cryst} \equiv (\text{crystalline})/(\text{crystalline} + \text{amorphous})$, for SW3-[B] ranges from $0.335^{+0.089}_{-0.112}$ at the nucleus, declining to $0.061^{+0.068}_{-0.061}$ at a cometocentric distance of $6.0''$ out into the coma in the anti-sunward direction. The f_{cryst} derived for SW3-[C] is $0.257^{+0.039}_{-0.043}$ towards the nucleus, declining to $0.0^{+0.073}_{-0.0}$ at a cometocentric distance of $5''$ into the coma in the anti-sunward direction. Therefore, within the 1-sigma confidence level, both fragments have a similar crystalline silicate fraction. For many EC comets and in

some NICs, the fraction of cometary grains that are Mg-rich is high ($f_{cryst} \simeq 0.08 - 0.3$). In 9P, $f_{cryst} \simeq 0.3$ was found in the post-impact coma (Harker et al. 2007; Sugita et al. 2005). Overall, lack of significant mineralogical differences between SW3 fragments may indicate that the original nucleus of the comet was generally homogeneous in composition as opposed to that of 1P/Halley or 9P (Wooden 2008).

The spectra of fragment SW3-[C] in the sunward direction are dominated by emission from amorphous pyroxene and carbon, with little to no emission from crystals (Table 3). The peak of the grain size distribution is also slightly larger ($0.5 - 1.3 \mu\text{m}$) compared with the derived values in the anti-sunward direction ($0.3 - 0.4 \mu\text{m}$), in addition to being more solid than the latter. We attribute these differences in the grain properties to the dynamics of the grains as they are released from the nucleus of fragment SW3-[C]. Smaller and/or more porous grains which can exhibit crystalline emission are more easily affected by the radiation pressure or are better coupled to and entrained in the sublimating gas (e.g., (Harker et al. 2007; Orosei et al. 1995)). Likely these grains are more easily swept out into the anti-sunward direction. However, a full dynamical analysis of the trajectory of the grains is outside the scope of this work.

The relative abundance of amorphous carbon in the anti-sunward coma of SW3-[B] ranges between $\simeq 45 - 23 \text{ wt}\%$, while for SW3-[C] the value ranges between $\simeq 60 - 42 \text{ wt}\%$. The wt% of amorphous carbon in both fragments varies a little with distance from the nucleus ($\simeq 20\%$) and is comparable to mean values deduced for other comets, especially ECs (10 to 50 wt%) comae (Wooden 2008). For example Harker et al. (2002, 2004) find amorphous carbon abundance (relative to other refractory materials) of 21 wt% for comet C/1995 O1 (Hale-Bopp), Wooden et al. (2004) cite 15 wt% for C/2001 Q4 (NEAT), while Harker et al. (2007) deduce a 28 wt% relative abundance for the pre-impact coma of 9P. Each of the later values (including those for SW3) were derived using the same discrete composition thermal model approach for SED decomposition, enabling a consistent comparison of relative abundances that are not model dependent (Wooden 2008).

The average silicate-to-carbon ratio in the extended anti-sunward coma for fragment SW3-[B] ranges between 1.156 – 3.43, while for fragment SW3-[C] the value ranges between 0.671 – 1.882. Overall, these ratios are comparable to values derived for other EC comets (Kelley et al. 2006; Harker et al. 2007; Lisse et al. 2006; Reach et al. 2010). Fragment SW3-[B] went through an outburst event just prior to our observations and this event could be responsible for the higher silicate-to-carbon ratio in fragment SW3-[B] compared to that of fragment SW3-[C], as well as the slight differences in the peak of the grain size distribution between the two fragments. The date of the outburst from fragment SW3-[B] has been estimated to have been between 2006 April 16 to 26 (Vincent et al. 2010). Likely, material

from the outburst is responsible for the region of enhanced flux in fragment SW3-[B] seen 3'' from the nucleus region in our images. The activity from fragment SW3-[C] is primarily from two active jets on the nucleus (Vincent et al. 2010) that could be preferentially ejecting small grains from the nucleus subsurface. On the other hand, fragment SW3-[B] was exhibiting fragmentation that released all subsurface grains in a single event. Therefore, in bulk, the grains released during a fragmentation event are slightly larger and more silicate rich than those entrained in the active jet outflows from the nucleus surface.

The radial difference in the silicate-to-carbon ratio in each fragment could arise from fragmentation of composite silicate rich grain aggregates entrained in the out flowing gas. Jones et al. (2008) observed fragments SW3-[B] and SW3-[C] in imaging polarimetry mode in the near-IR, finding that the surface brightnesses of both fragments are consistent with significant grain fragmentation. Their model requires a factor of 10 change in the mean grain size within 2–200 km from the nucleus (corresponding to 2'' in our Michelle observations). In addition, the scattered light polarization profile slightly increased over the same distances. The latter observations suggest that the grains were fragmenting, although the polarization could have also increased from the release of volatiles such as water ice and organics, which may change the light scattering properties of the grains (Jones et al. 2008). Despite the evidence for fragmentation in the scattered light, the grain size distribution derived from our thermal models do not appreciably vary, nor does a_p . Our best-fit grain size distributions have $N = 3.4$. This shallow power-law slope suggests that the scattered light could be dominated by the largest grains which are too cool to be seen in the 10 μm region. Because smaller grains have higher radiative equilibrium temperatures, the mid-IR emission at 10 μm may be dominated by $\sim 0.1 - 1 \mu\text{m}$ grains (Reach et al. 2007). Therefore the two datasets may not be so incongruent if the largest grains, perhaps 10s or 100s of μm in size, are fragmenting, but do not significantly affect the 8–13 SED because of their cool radiative equilibrium temperatures.

Alternatively, the increase in silicate-to-carbon ratio with distance from the nucleus could be due to grain sorting in the coma. In this scenario, the more transparent silicate species would dynamically separate from the dark amorphous carbon grains. Moderately porous ($D = 2.857$) amorphous carbon grains have a 2–3 times larger response to radiation pressure than do the same-sized silicate grains (Kelley 2006). Grain sorting by size and mineral composition was suggested from the time-of-flight analysis of the 9P post-impact coma contaminated by material from the ejecta plume (Harker et al. 2007).

4.2. Comparison to Other Comets

It is instructive to compare the spectral signature of coma dust in the environs of the SW3 fragments to other comets observed at mid-IR wavelengths to place the conclusion based on thermal model analysis and mineral decomposition analysis in context. Fig. 5 is a composite plot of the spectra of fragments SW3-[B], SW3-[C], comets C/1995 O1 (Hale-Bopp), 9P post-Deep Impact, and C/2001 Q4 (NEAT) observed with ground-based mid-IR spectrographs, C/2004 B1 (LINEAR) and 17P/Holmes observed with *Spitzer* IRS spectrograph; and 1P/Halley observed by the Kupier Airborne Observatory. Comets C/1995 O1 (Hale-Bopp) and 17P/Holmes (17P) clearly have the strongest silicate features (defined as the excess over the blackbody continuum). However, we note that 17P was observed by *Spitzer* a little more than a couple of weeks after an extremely violent outburst event. This material was still within the *Spitzer* IRS spectral beam, and is therefore the reason for the relatively large silicate feature. The grains in the coma of C/1995 O1 (Hale-Bopp) were fractally very porous ($D = 2.5$) with the HGSD peaking at $a_p = 0.2 \mu\text{m}$ (Harker et al. 2002). The coma dust in C/1995 O1 (Hale-Bopp) is also mineralogically diverse and includes amorphous and crystalline forms of both olivine and pyroxene (Harker et al. 2002). Similarly, the dust ejected from 9P post-Deep Impact was also mineralogically diverse and small ($a_p = 0.2 \mu\text{m}$) in size, although the grains were moderately fractally porous ($D = 2.727$) (Harker, Woodward, & Wooden 2005). Furthermore, comet C/2001 Q4 (NEAT) also displayed a mineralogically diverse grain population, however, the grains were solid ($D = 3.0$) and slightly larger than those in Hale-Bopp and 9P ($a_p = 0.3 \mu\text{m}$) (Wooden et al. 2004).

Comet 17P/Holmes also was observed to have distinct Mg-rich crystalline olivine features at $11.2 \mu\text{m}$ and $11.9 \mu\text{m}$ in apertures centered on the nucleus and in the diffuse coma, as well as toward the isolated dust cloud arising from the violent outburst event (Reach et al. 2010; Watanabe et al. 2010). In 17P, dust producing these $10 \mu\text{m}$ features may arise from fluffy aggregate complexes containing small Mg-rich crystalline silicates (e.g., Kimura et al. 2008), or small silicates ($a \lesssim 0.1 \mu\text{m}$) admixed larger amorphous dust. Sharp crystalline silicate features from small grains superposed on a thermal continuum arising from larger amorphous carbonaceous and silicate species in the $10 \mu\text{m}$ SED were evident in remote sensing observations of comet 1P/Halley by the Kupier Airborne Observatory (Bregman et al. 1987), while the *in situ* flyby measurement through the coma (McDonnell et al. 1987) indicated that the grain sized distribution was dominated by large $\simeq 1 \mu\text{m}$ sized particles. Comet C/2004 B1 (LINEAR) has a relatively weak and featureless silicate feature indicative of emission from a large ($> 1 \mu\text{m}$) grain population.

While there are similarities in dust grain characteristics between C/1995 O1 (Hale-Bopp), 9P, and 17P possibly a signature of a common formation zone in the solar nebula of

the parent body aggregates for these comets, the composition of SW3 seems distinctly different. As SW3 fragmented into many pieces that subsequently sublimated leading to outbursts of gas entrained with dust particles from within the bulk interior of the original nucleus (natural excavation at depth akin to the subsurface penetration of Deep Impact projectile), surface weather effects cannot be invoked to explain dissimilarities in grain properties. ECs with frequent perihelion passages and low semi-major orbital axis are thought to have coma grain populations dominated by larger, compact dust particles arising from highly processed surface layers constituting the nucleus crust (Priyalnik & Mekler 1991) as opposed to the more pristine grains released in active Oort cloud comets. Larger grains are necessary to explain the aperture-dependent polarization properties and low total polarization (\lesssim few percent) of some ECs (Jones et al. 2008; Kolokolova et al. 2007). However, SW3 has an unusually high polarization for an EC in both the optical and near-IR at a range of phase angles, which lead Jones et al. (2008) to suggest that observational feature is best explained by the release of unprocessed, porous aggregates with small effective radii from the interior of disintegrating comet nuclei.

Although fragment SW3-[B] underwent an outburst event revealing pristine grains from the nucleus interior, the grain properties and mineralogy of its dust does not resemble that of either 9P or of Hale-Bopp. This dissimilarity could be attributed to 1) the smaller, more porous dust grains traveling out of the coma of fragment SW3-[B] prior to our observations; or 2) the dust properties of SW3 *fundamentally differ* from that of 9P (and Hale-Bopp) implying a different formation process or evolutionary history. However, the former conjecture is ruled out by polarimetric observations and dust fragmentation studies of the SW3-[B] coma (Jones et al. 2008) obtained at epochs contemporaneous with our mid-IR spectrophotometry.

5. CONCLUSIONS

Mid-IR images and spectroscopic observations of the ecliptic (Jupiter family) comet 73P/Schwassman-Wachmann 3, fragments SW3-[B] and SW3-[C], were analyzed using thermal emission models. Based on our modeling, the comae dust, and by inference the bulk internal properties, of the individual fragments are similar with the observed mid-IR flux being dominated by emission from amorphous pyroxene and amorphous carbon, with evidence for emission from amorphous olivine towards the nucleus in both fragments. Emission from both fragments shows evidence for the existence of some crystalline olivine in the extended coma in the anti-sunward direction. The grain properties in both fragments are also similar: solid to moderately porous grains ($D = 3.0 - 2.727$) with a large grain slope of $N = 3.4$ and the peak of the HGSD ranging between 0.3 and $\sim 1.0 \mu\text{m}$. Finally, the two fragments

exhibit a similar, but slightly different silicate-to-carbon ratio (1.341 for SW3-[B] and 0.671 for SW3-[C]); a ratio equivalent to those found for other ECs. The slight differences in grain size distribution and silicate-to-carbon ratio between the two fragments likely arises because SW3-[B] was actively fragmenting throughout its passage while the activity in SW3-[C] was primarily driven by jets. The breakup event populated the coma of fragment SW3-[B] with subsurface material. Conversely, for fragment SW3-[C], the dust population of its coma was driven by two active jets.

There are other differences between the two fragments, including the detection in fragment SW3-[B] of orthopyroxene in both the sunward and anti-sunward directions. In fragment SW3-[C], orthopyroxene is primarily detected in only the sunward direction. The crystalline silicate fraction is higher in SW3-[B] than in SW3-[C] based on constraints derived for the crystalline silicate fraction from thermal modelling of the SEDs. Although f_{cryst} for both fragments is similar to the range of f_{cryst} inferred for other ECs.

Comparison of coma dust properties of 73P to those of derived for ecliptic comet 9P/Tempel 1 just after the Deep Impact event, and to the archetypal, “pristine” nearly-isotropic (Oort cloud) comet C/1995 O1 (Hale-Bopp) suggests that materials released from fragment SW3-[B] which may expose grain material buried at depth below the surface of the original larger nucleus is devoid of very small ($a \leq 0.5 \mu\text{m}$) dust grains. The apparent absence, or diminished population of such small grain species may either be a result of dynamical sorting whereby this population has passed out of the coma before our observations, or more likely, the initial parent body makeup of 73P is different than that of 9P/Tempel 1 or even C/1995 O1 (Hale-Bopp).

Data discussed in this manuscript are based on observations obtained at the Gemini Observatory, which is operated by the Association of Universities for Research in Astronomy, Inc., under a cooperative agreement with the NSF on behalf of the Gemini partnership: the National Science Foundation (United States), the Science and Technology Facilities Council (United Kingdom), the National Research Council (Canada), CONICYT (Chile), the Australian Research Council (Australia), Ministério da Ciência e Tecnologia (Brazil) and Ministerio de Ciencia, Tecnología e Innovación Productiva (Argentina). DEH and CEW acknowledge support for this work from the National Science Foundation grant AST-0706980. DEH, DHW and CEW also acknowledge partial support for this work from NASA Planetary Astronomy Grant RTOP 344-32-21-04. MSK acknowledges support from NASA Planetary Astronomy Grant NNX09AF10G. The authors also would like to thank the Gemini Observatory staff for their support in conducting these observations as well as an anonymous referee whose comments improved the manuscript.

REFERENCES

- Alistair C. G., Etedgui-Atad, E., & Harris, J.W. 1997, Proc. SPIE 2871, 1197
- A'Hearn, M. F., et al. 1995, *Icarus*, 118, 223
- Bazell, D., & Dwek, E. 1990, *ApJ*, 360, 142
- Belton, M. J. S., et al. 2006, *Icarus*, 187, 332
- Bockelée-Morvan, D., et al. 2002, *A&A*, 384, 1107
- Bradley, J. P., Snow, T. P., Brownlee, D. E., & Hanner, M. S. 1999, in *Solid Interstellar Matter: The ISO Revolution, Les Houches Workshop, February 2-6, 1998*, Eds. L. d'Hendecourt, C. Joblin, and A. Jones (EDP Sciences, Springer-Verlag: Berlin), p.298
- Bradley, J. P. 1994, *Science*, 265, 925
- Bregman, J. D., Witteborn, F. C., Allamandola, L. J., Campins, H., Wooden, D. H., Rank, D. M., Cohen, M., & Tielens, A. G. G. M. 1987, *A&A*, 187, 616
- Brownlee, D., et al. 2006, *Science*, 314, 1711
- Boss, A. P. 2004, *ApJ*, 616, 1265
- Chihara, H., Koike, C., Tsuchiyama A., Tachibana, S., & Sakamoto, D. 2002, *A&A*, 391, 267
- Ciesla, F. J. 2007. Outward Transport of High-Temperature Materials Around the Midplane of the Solar Nebula. *Science* 318, 613.
- Cohen, M., Witteborn, F. C., Carbon, D. F., Davies, J. K., Wooden, D. H., & Bregman, J. D. 1996, *AJ*, 112, 2274
- Crovisier, J. 2007, in *Planetary Sciences: Challenges and Discoveries*, astro-ph/073758
- Crovisier, J., Bockelée-Morvan, D., Gerard, E., Rauer, H., Biver, N., Colom, P., & Jorda, L. 1996, *A&A*, 310, L17
- Crovisier, J., and 13 colleagues 2000. Thermal Emission Spectroscopy and Analysis of Dust, Disks, and Regoliths 196, 109-117.
- Crovisier, J., 1999, in *The Universe as Seen by ISO, ESA-SP 427*, 161

- Crovisier, J., Leech, K., Bockelée-Morvan, D., Brooke, T. Y., Hanner, M. S., Altieri, B., Keller, H. U., & Lellouch, E. 1997, *Science*, 275, 1904
- Cuzzi, J. N., et al. 1993, *Icarus*, 106, 102
- Dello Russo, N., Vervack, R. J., Weaver, H. A., Biver, N., Bockelée-Morvan, D., Crovisier, J., & Lisse, C. M. 2007, *Nature*, 448, 172
- Dorschner, J., Begemann, B., Henning, T., Jaeger, C., & Mutschke, H. 1995. *A&A*, 300, 503
- Ebel, D. S., et al. 2006, *DPS* 38, #13.19
- Edoh, O. 1983, Ph.D. Thesis, University of Arizona.
- Ehrenfreund, P., et al. 2004, in *Comets II*, eds. M. Festou, et al., (Tucson, AZ: U. Arizona Press), p.115
- Fabian, D., Henning, T., Jäeger, C., Mutschke, H., Dorschner, J., & Wehrhan, O. 2001, *A&A*, 378, 228
- Fernandez, J. A. & Ip, W.-H. 1981, *Icarus*, 47, 470
- Gomes, R. S. 2003, *Icarus*, 161, 404
- Grossman, L. 1972. Condensation in the primitive solar nebula. *Geochimica et Cosmochimica Acta* 36, 597-619.
- Gehrz, R. D., Roellig, T. L., Werner, M. W., Fazio, G. G., Houck, J. R., Low, F. J., Rieke, G. H., Sofier, B. T., Levine, D. A., & Romana, E. A. 2007, *Rev. Scientific Instruments* 78, 1302
- Hallenbeck, S. L., et al. 1998, *Icarus*, 131, 193
- Hanner, M. S. & Zolensky, M. E. 2010, in *Astromineralogy*, 2nd Edition, ed. Th. Henning, Springer Verlag, in press.
- Hanner, M. S. & Bradley, J. P. 2004, in *Comets II*, eds. M. Festou, et al. (Tucson, AZ: U. Arizona Press), p.555
- Hanner, M. S., Lynch, D. K., & Russell, R. W. 1994, *ApJ*, 425, 274
- Harker, D. E., Woodward, C. E., Wooden, D. H., Fisher, R. S., & Trujillo, C. 2007, *Icarus*, 191, 432
- Harker, D. E., Woodward, C. E., Wooden, D. H., 2005 *Science* 310, 278-280.

- Harker, D. E., Wooden, D. H., Woodward, C. E., & Lisse, C. M. 2004, *ApJ*, 615, 1081 errata
- Harker, D. E., Wooden, D. H., Woodward, C. E., & Lisse, C. M. 2002, *ApJ*, 580, 579
- Harker, D. E. & Desch, S. 2002, *ApJ*, 565, L109
- Harker, D. E., Woodward, C. E., & Wooden, D. E. 2005, *Science*, 310, 278
- Harris, A. W. 1998, *Icarus*, 131, 291
- Howell, E. S., Nolan, M. C., Harmon, J. K., Lovell, A. J., Benner, L. A., Ostro, S. J., Campbell, D. B., & Margot, J. 2007, *Bulletin of the American Astronomical Society*, 38, 486
- Jäger, C., Molster, F. J., Dorschner, J., Henning, T., Mutschke, H., & Waters, L. B. F. M. 1998, *A&A*, 339, 904
- Jones, T. J., Stark, D., Woodward, C. E., Kelley, M. S., Kolokolova, L., Clemens, D., & Pinnick, A. 2008, *AJ*, 135, 1318
- Joyce, R. R. 1992. *Observing With Infrared Arrays*. ASP Conf. Ser. 23: *Astronomical CCD Observing and Reduction Techniques* 23, p.258
- Kelley, M. S., & Wooden, D. H. 2009, *Planetary Spac. Sci.*, 57, 1133
- Kelley, M. S., et al. 2006, *ApJ*, 651, 1256
- Kelley, M. S. 2006, Ph.D. Thesis, University of Minnesota
- Kemper, F., Vriend, W. J., & Tielens, A. G. G. M. 2005, *ApJ*, 633, 534
- Kemper, F., Vriend, W. J., Tielens, A. G. G. M. 2004. *The Absence of Crystalline Silicates in the Diffuse Interstellar Medium*. *Astrophysical Journal* 609, 826-837.
- Kiselev, N., Jockers, K., & Rosenbush, V. 2002, *Earth, Moon, Planets*, 90, 167
- Koike C., Chihara, H., Tsuchiyzma, A., Suto, H., Sogawa, H., & Okuda, H. 2003, *A&A*, 399, 1101
- Kimura, H., Chigai, T., & Yamamoto, T. 2008, *A&A*, 482, 305
- Kolokolova, L., Kimura, H., Kiselev, N., & Rosenbush, V. 2007, *A&A*, 463, 1189
- Levison, H. F. & Morbidelli, A. 2003, *Nature*, 426, 419

- Li, A., & Draine, B. T. 2001, *ApJ*, 550, L213
- Lisse, C. M., et al. 2006, *Science* 313, 635-640.
- Lisse, C. M., A’Hearn, M. F., Hauser, M. G., Kelsall, T., Lien, D. J., Moseley, S. H., Reach, W. T., & Silverberg, R. F. 1998, *ApJ*, 496, 971
- Lord, S. D. 1993, NASA Techn. Rep. TM-103957 (Moffet Field: NASA/Ames Research Center)
- McDonnell, J. A. M., et al. 1987, *A&A*, 187, 719
- Meech, K. & Svoren 2004, in *Comets II*, eds. M. Festou, et al. (Tucson, AZ: U. Arizona Press), p.317
- Min, M., Hovenier, J. W., de Koter, A., Waters, L. B. F. M., & Dominik, C. 2005, *Icarus* 179, 158
- Morbidelli, A., Emel’yanenko, V. V., & Levison, H. F. 2004, *MNRAS*, 355, 935
- Morbidelli, A. & Levison, H. F. 2003, *Nature*, 422, 30
- Moreno, F., Muñoz, O., Vilaplana, R., & Molina, A. 2003, *ApJ*, 595, 522
- Oört, J. 1950, *Bull. Ast. Inst. Neth.*, 11, 91
- Orosei, R., Capaccioni, F., Capria, M. T., Coradini, A., Espinasse, S., Federico, C., Salomone, M., & Schwehm, G. H. 1995, *A&A*, 301, 613
- Pan, M. & Sari, R. 2005, *Icarus*, 173, 342
- Prialnik, D., & Mekler, A. 1991, *ApJ*, 366, 318
- Reach, W. T., et al. 2010, arXiv:1001.4161v2
- Reach, W. T., Vaubaillon, J., Kelley, M. S., Lisse, C. M., & Sykes, M. V. 2009, *Icarus*, 203, 571
- Reach, W. T., Kelley, M. S., & Sykes, M. V. 2007, *Icarus*, 191, 298
- Scotti, J. V., Galad, A., Boehnhardt, H., Kaufl, H. U., Chen, J., Jewitt, D., Reinsch, K., Storm, J., & Sekanina, Z. 1996, *IAU Circ.*, 6301, 1
- Sekanina, Z. 2005, *International Comet Quarterly*, 27, 225

- Sitko, M. L., Lynch, D. K., Russell, R. W., & Hanner, M. S. 2004, *ApJ*, 612, 576
- Stansberry, J. A., and 17 colleagues, 2004. Spitzer Observations of the Dust Coma and Nucleus of 29P/Schwassmann-Wachmann 1. *Astrophysical Journal Supplement Series* 154, 463-468.
- Stern, S. A. 2003, *Nature*, 424, 639
- Sugita, S. et al. 2005, *Science* 310, 274
- Vincent, J.-B., Bönhardt, H., Bertini, I., Lara, L.-M., Küppers, M., & Rodrigo, R. 2010, *Earth Moon and Planets*, 106, 27
- Watanabe, J., et al. 2009, *Pub. Astron. Soc. Japan*, 61, 679
- Watanabe, J., Kawakita, H., Honda, M., Ootsubo, T., Fuse, T., Yamashita, T., Furusho, R., Kasuga, T., 2005. *IAU Symposium Abstracts* 229, 121.
- Weaver, H. A., et al. 2008, *Asteroids, Meteor, Comets*, LPI Contr. 104.8248W
- Weaver, H. A., et al. 1995, *Science*, 267, 1282
- Werner, M. W. Fazio, G., Rieke, G., Roellig, T. L., & Watson, D. M. 2006, *Ann. Rev. of Astronomy and Astrophysics* 44, 269
- Whitman, K., Morbidelli, A., & Jedicke, R. 2006, *Icarus*, 183, 101
- Wooden, D. H. 2008, *Space Sci. Rev.*, 138, 75
- Wooden, D. H. 2005, in *Highlights of Astronomy*, Vol. 13, eds. O. Engvold, (San Francisco, CA: Astron. Soc. Pacific), p.495
- Wooden, D. H., et al. 2007, in *PPV*, eds. B. Reipurth, et al., (Univ. Arizona Press: Tucson), p.815
- Wooden, D. H., Woodward, C. E., & Harker, D. E. 2004, *ApJ*, 612, L77
- Wooden, D. H., 2002. *Comet Grains: Their IR Emission and Their Relation to ISM Grains*. *Earth Moon and Planets* 89, 247-287.
- Wooden, D. H., Butner, H. M., Harker, D. E., & Woodward, C. E. 2000, *Icarus* 143, 126
- Wooden, D. H., Harker, D. E., Woodward, C. E., Butner, H. M., Koike, C., Witteborn, F. C., & McMurtry, C. W. 1999, *ApJ*, 517, 1034

Wooden, D. H. 1979, Ph.D Thesis, Univ. California, Santa Cruz.

Table 1. MICHELLE OBSERVATIONAL SUMMARY

UT Date	Start Time ^a (hr:min)	Frag.	Airmass of Comet	Int. Time ^b (sec)	Flux Standard	Airmass of Standard	r_h (AU)	Δ (AU)	Data Obtained ^c	Flux ^f (Jy)
29 Apr 2006	12:21	[B]	1.039	54.4	HD127665	1.065	1.110	0.154	18.1 μm image	13.60 ± 0.33
29 Apr 2006	12:23	[B]	1.043	51.8	HD127665	1.072	1.110	0.154	11.6 μm image	6.54 ± 0.07
29 Apr 2006	12:41	[B]	1.104	806.4	HD127665	1.096	1.110	0.154	Low N ^d	...
29 Apr 2006	13:55	[B]	1.199	756.0	HD156283	1.151	1.110	0.154	Low Q ^d	...
30 Apr 2006	11:36	[C]	1.043	54.4	HD156283	1.151	1.085	0.129	18.1 μm image	41.64 ± 1.00
30 Apr 2006	11:42	[C]	1.039	51.8	HD156283	1.048	1.085	0.129	11.6 μm image	30.10 ± 0.30
30 Apr 2006	12:57	[C]	1.034	302.4	HD156283	1.056	1.085	0.129	Low N ^e	...

^a Start time of integration.

^b Integration time on-source.

^c Low N = Low-Res 10 μm spectrum; Low Q = Low-Res 20 μm spectrum.

^d Slit rotated to position angle = 25°

^e Slit rotated to position angle = 45°

^f Flux in a 7.44'' diameter aperture centered on the peak isophote of the surface brightness distribution.

Table 2. BEST-FIT THERMAL EMISSION MODEL PARAMETERS FOR FRAGMENT B

Extraction ^a Aperture	Offset ^b (arcsec)	N	M	a_p ^c	D	$N_p(\times 10^{16})$					χ^2_ν
						Amorphous Pyroxene	Amorphous Olivine	Amorphous Carbon	Crystalline Olivine	Ortho- Pyroxene	
A	+1	3.4	27.20	0.9	3.000	0.643 ^{+0.009} _{-0.011}	0.000 ^{+0.003} _{-0.000}	0.000 ^{+0.007} _{-0.000}	0.000 ^{+0.047} _{-0.000}	0.854 ^{+0.233} _{-0.233}	2.71
B	0	3.4	13.60	0.5	2.727	3.310 ^{+0.989} _{-0.989}	0.782 ^{+0.461} _{-0.463}	9.703 ^{+0.327} _{-0.330}	0.686 ^{+0.701} _{-0.686}	2.648 ^{+1.338} _{-1.311}	0.75
C	-1	3.4	13.60	0.5	3.000	2.671 ^{+0.312} _{-0.312}	0.000 ^{+0.036} _{-0.000}	5.296 ^{+0.213} _{-0.213}	0.268 ^{+0.310} _{-0.268}	1.701 ^{+0.554} _{-0.554}	1.14
D	-2	3.4	10.20	0.4	2.857	5.933 ^{+0.626} _{-0.639}	0.000 ^{+0.196} _{-0.000}	9.800 ^{+0.370} _{-0.369}	0.980 ^{+0.439} _{-0.439}	1.540 ^{+0.859} _{-0.850}	1.04
E	-3	3.4	13.60	0.5	2.857	3.621 ^{+0.361} _{-0.367}	0.000 ^{+0.025} _{-0.000}	4.913 ^{+0.223} _{-0.223}	0.170 ^{+0.350} _{-0.170}	1.481 ^{+0.651} _{-0.650}	1.55
F	-4	3.4	13.60	0.5	3.000	2.827 ^{+0.310} _{-0.309}	0.000 ^{+0.070} _{-0.000}	4.837 ^{+0.213} _{-0.214}	0.393 ^{+0.306} _{-0.311}	2.159 ^{+0.554} _{-0.555}	1.00
G	-5	3.4	13.60	0.5	3.000	3.949 ^{+0.302} _{-0.302}	0.000 ^{+0.038} _{-0.000}	3.101 ^{+0.207} _{-0.208}	0.409 ^{+0.285} _{-0.285}	1.145 ^{+0.521} _{-0.520}	1.38
H	-6	3.4	13.60	0.5	3.000	4.494 ^{+0.269} _{-0.277}	0.000 ^{+0.022} _{-0.000}	1.877 ^{+0.191} _{-0.191}	0.000 ^{+0.245} _{-0.000}	0.384 ^{+0.474} _{-0.384}	3.46

^a Label of spectral extraction aperture (see Fig. 2)

^b Distance that the center of the $0.''6 \times 1.0''$ extraction box is offset from the peak brightness. A positive value indicates an offset in the N-E direction, and a negative value indicates an offset in the S-W direction (see Fig. 2). Both offsets are along the slit orientation axis of PA = -25 (see text).

^c Derived parameter

^d Bold values indicate values constrained to a confidence level of 1-sigma.

Table 3. BEST-FIT THERMAL EMISSION MODEL PARAMETERS FOR FRAGMENT C

Extraction ^a Aperture	Offset ^b (arcsec)	N	M	a_p ^c	D	Amorphous Pyroxene	Amorphous Olivine	$N_p(\times 10^{16})$ Amorphous Carbon	Crystalline Olivine	Ortho- Pyroxene	χ_ν^2
I	+4	3.4	13.60	0.5	3.000	2.619 ^{+0.239} _{-0.241}	0.000 ^{+0.025} _{-0.000}	0.480 ^{+0.190} _{-0.194}	0.000 ^{+0.044} _{-0.000}	0.000 ^{+0.225} _{-0.000}	2.79
J	+3	3.4	13.60	0.5	3.000	3.000 ^{+0.285} _{-0.361}	0.000 ^{+0.029} _{-0.000}	1.287 ^{+0.251} _{-0.221}	0.000 ^{+0.042} _{-0.000}	0.070 ^{+0.541} _{-0.070}	2.58
K	+2	3.4	10.20	0.4	3.000	7.113 ^{+0.870} _{-0.887}	0.000 ^{+0.089} _{-0.000}	6.789 ^{+0.571} _{-0.567}	0.000 ^{+0.159} _{-0.000}	0.903 ^{+1.081} _{-0.903}	2.44
L	+1	3.4	40.80	1.3	2.727	0.692 ^{+0.078} _{-0.078}	0.000 ^{+0.002} _{-0.000}	0.483 ^{+0.049} _{-0.048}	0.000 ^{+0.114} _{-0.000}	4.747 ^{+2.902} _{-2.888}	4.00
M	0	3.4	6.80	0.3	2.727	0.000 ^{+2.208} _{-0.000}	34.910 ^{+3.640} _{-3.610}	190.800 ^{+3.600} _{-3.600}	37.150 ^{+7.660} _{-7.660}	0.000 ^{+1.227} _{-0.000}	3.28
N	-1	3.4	6.80	0.3	2.727	6.784 ^{+9.496} _{-6.784}	20.900 ^{+4.040} _{-4.500}	65.350 ^{+2.470} _{-2.410}	6.397 ^{+3.370} _{-3.341}	0.000 ^{+5.330} _{-0.000}	0.46
O	-2	3.4	10.20	0.4	2.727	10.640 ^{+1.480} _{-2.033}	0.000 ^{+0.896} _{-0.000}	12.420 ^{+0.690} _{-0.690}	2.690 ^{+0.971} _{-1.046}	1.451 ^{+2.189} _{-1.451}	0.71
P	-3	3.4	6.80	0.3	2.857	22.350 ^{+2.410} _{-5.220}	0.357 ^{+2.443} _{-0.357}	20.600 ^{+1.660} _{-1.310}	2.624 ^{+1.357} _{-1.456}	0.000 ^{+2.747} _{-0.000}	0.65
Q	-4	3.4	6.80	0.3	2.857	12.450 ^{+4.090} _{-4.429}	1.277 ^{+2.065} _{-1.277}	16.870 ^{+1.450} _{-1.440}	1.137 ^{+1.189} _{-1.137}	0.816 ^{+2.429} _{-0.816}	0.91
R	-5	3.4	6.80	0.3	2.857	12.900 ^{+1.150} _{-1.510}	0.000 ^{+0.478} _{-0.000}	12.200 ^{+0.890} _{-0.830}	0.000 ^{+0.357} _{-0.000}	0.000 ^{+1.292} _{-0.000}	1.24

^a Same as for Table 2

^b Same as for Table 2

^c Derived parameter

^d Bold values indicate values constrained to a confidence level of 1-sigma.

Table 4. MASS OF SUBMICRON GRAINS FOR FRAGMENT B

Extraction Aperture	Total Mass ($\times 10^2$ kg)	Amorphous Pyroxene	Mass Relative to Total Mass				Orthopyroxene	Silicate/Carbon	f_{cryst}^a
			Amorphous Olivine	Amorphous Carbon	Crystalline Olivine				
A	$0.456^{+0.069}_{-0.069}$	$0.430^{+0.082}_{-0.061}$	$0.000^{+0.002}_{-0.000}$	$0.000^{+0.003}_{-0.000}$	$0.000^{+0.030}_{-0.000}$	$0.570^{+0.061}_{-0.082}$...	$0.570^{+0.061}_{-0.082}$	
B	$2.300^{+0.288}_{-0.282}$	$0.192^{+0.060}_{-0.059}$	$0.045^{+0.032}_{-0.028}$	$0.427^{+0.052}_{-0.041}$	$0.069^{+0.060}_{-0.069}$	$0.266^{+0.090}_{-0.113}$	$1.341^{+0.250}_{-0.253}$	$0.335^{+0.089}_{-0.112}$	
C	$1.999^{+0.099}_{-0.098}$	$0.309^{+0.048}_{-0.045}$	$0.000^{+0.004}_{-0.000}$	$0.464^{+0.014}_{-0.013}$	$0.031^{+0.034}_{-0.031}$	$0.197^{+0.052}_{-0.057}$	$1.156^{+0.063}_{-0.065}$	$0.228^{+0.051}_{-0.056}$	
D	$2.083^{+0.108}_{-0.106}$	$0.355^{+0.054}_{-0.049}$	$0.000^{+0.012}_{-0.000}$	$0.445^{+0.014}_{-0.013}$	$0.078^{+0.031}_{-0.033}$	$0.122^{+0.059}_{-0.064}$	$1.248^{+0.068}_{-0.069}$	$0.200^{+0.057}_{-0.063}$	
E	$1.655^{+0.129}_{-0.129}$	$0.379^{+0.065}_{-0.059}$	$0.000^{+0.003}_{-0.000}$	$0.390^{+0.022}_{-0.019}$	$0.024^{+0.045}_{-0.024}$	$0.207^{+0.069}_{-0.081}$	$1.564^{+0.132}_{-0.137}$	$0.231^{+0.072}_{-0.084}$	
F	$2.090^{+0.099}_{-0.099}$	$0.313^{+0.046}_{-0.043}$	$0.000^{+0.008}_{-0.000}$	$0.405^{+0.011}_{-0.010}$	$0.043^{+0.032}_{-0.034}$	$0.239^{+0.048}_{-0.053}$	$1.468^{+0.061}_{-0.065}$	$0.282^{+0.046}_{-0.050}$	
G	$1.815^{+0.092}_{-0.093}$	$0.503^{+0.058}_{-0.054}$	$0.000^{+0.005}_{-0.000}$	$0.299^{+0.013}_{-0.014}$	$0.052^{+0.034}_{-0.036}$	$0.146^{+0.056}_{-0.062}$	$2.342^{+0.159}_{-0.137}$	$0.198^{+0.054}_{-0.060}$	
H	$1.456^{+0.083}_{-0.068}$	$0.713^{+0.067}_{-0.068}$	$0.000^{+0.004}_{-0.000}$	$0.226^{+0.017}_{-0.019}$	$0.000^{+0.038}_{-0.000}$	$0.061^{+0.068}_{-0.061}$	$3.430^{+0.402}_{-0.313}$	$0.061^{+0.068}_{-0.061}$	

^a) Defined as $f_{cryst}^{silicates} \equiv (\text{crystalline})/(\text{crystalline} + \text{amorphous})$.

Table 5. MASS OF SUBMICRON GRAINS FOR FRAGMENT C

Extraction Aperture	Total Mass ($\times 10^2$ kg)	Mass Relative to Total Mass					Orthopyroxene	Silicate/Carbon	f_{cryst}^a
		Amorphous Pyroxene	Amorphous Olivine	Amorphous Carbon	Crystalline Olivine				
I	0.689 ^{+0.037} _{-0.021}	0.878 ^{+0.051} _{-0.081}	0.000 ^{+0.008} _{-0.000}	0.122 ^{+0.054} _{-0.051}	0.000 ^{+0.015} _{-0.000}	0.000 ^{+0.072} _{-0.000}	7.200 ^{+5.980} _{-2.503}	0.000 ^{+0.072} _{-0.000}	
J	0.935 ^{+0.090} _{-0.012}	0.742 ^{+0.061} _{-0.124}	0.000 ^{+0.007} _{-0.000}	0.241 ^{+0.037} _{-0.044}	0.000 ^{+0.010} _{-0.000}	0.017 ^{+0.120} _{-0.017}	3.148 ^{+0.918} _{-0.549}	0.017 ^{+0.120} _{-0.017}	
K	2.174 ^{+0.113} _{-0.094}	0.541 ^{+0.082} _{-0.080}	0.000 ^{+0.007} _{-0.000}	0.391 ^{+0.026} _{-0.027}	0.000 ^{+0.012} _{-0.000}	0.069 ^{+0.075} _{-0.069}	1.559 ^{+0.187} _{-0.159}	0.069 ^{+0.075} _{-0.069}	
L	1.065 ^{+0.575} _{-0.573}	0.072 ^{+0.097} _{-0.029}	0.000 ^{+0.000} _{-0.000}	0.038 ^{+0.039} _{-0.012}	0.000 ^{+0.021} _{-0.000}	0.890 ^{+0.041} _{-0.136}	25.228 ^{+11.706} _{-13.266}	0.890 ^{+0.041} _{-0.136}	
M	13.240 ^{+0.640} _{-0.630}	0.000 ^{+0.009} _{-0.000}	0.144 ^{+0.018} _{-0.017}	0.598 ^{+0.029} _{-0.026}	0.257 ^{+0.039} _{-0.043}	0.000 ^{+0.008} _{-0.000}	0.671 ^{+0.076} _{-0.076}	0.257 ^{+0.039} _{-0.043}	
N	4.817 ^{+0.423} _{-0.365}	0.077 ^{+0.096} _{-0.077}	0.238 ^{+0.065} _{-0.065}	0.563 ^{+0.052} _{-0.053}	0.122 ^{+0.050} _{-0.059}	0.000 ^{+0.093} _{-0.000}	0.775 ^{+0.183} _{-0.150}	0.122 ^{+0.095} _{-0.059}	
O	2.626 ^{+0.294} _{-0.228}	0.392 ^{+0.090} _{-0.080}	0.000 ^{+0.036} _{-0.000}	0.347 ^{+0.034} _{-0.024}	0.169 ^{+0.047} _{-0.056}	0.091 ^{+0.115} _{-0.091}	1.882 ^{+0.216} _{-0.259}	0.261 ^{+0.104} _{-0.098}	
P	2.921 ^{+0.184} _{-0.184}	0.535 ^{+0.047} _{-0.104}	0.009 ^{+0.063} _{-0.009}	0.374 ^{+0.045} _{-0.031}	0.082 ^{+0.038} _{-0.044}	0.000 ^{+0.081} _{-0.000}	1.675 ^{+0.245} _{-0.287}	0.082 ^{+0.083} _{-0.044}	
Q	2.034 ^{+0.173} _{-0.186}	0.428 ^{+0.124} _{-0.138}	0.044 ^{+0.083} _{-0.044}	0.440 ^{+0.061} _{-0.048}	0.051 ^{+0.046} _{-0.051}	0.037 ^{+0.098} _{-0.037}	1.275 ^{+0.277} _{-0.279}	0.088 ^{+0.105} _{-0.073}	
R	1.549 ^{+0.069} _{-0.027}	0.582 ^{+0.037} _{-0.070}	0.000 ^{+0.022} _{-0.000}	0.418 ^{+0.031} _{-0.037}	0.000 ^{+0.021} _{-0.000}	0.000 ^{+0.073} _{-0.000}	1.395 ^{+0.232} _{-0.166}	0.000 ^{+0.073} _{-0.000}	

^{a)}Defined as $f_{cryst}^{silicates} \equiv (\text{crystalline})/(\text{crystalline} + \text{amorphous})$.

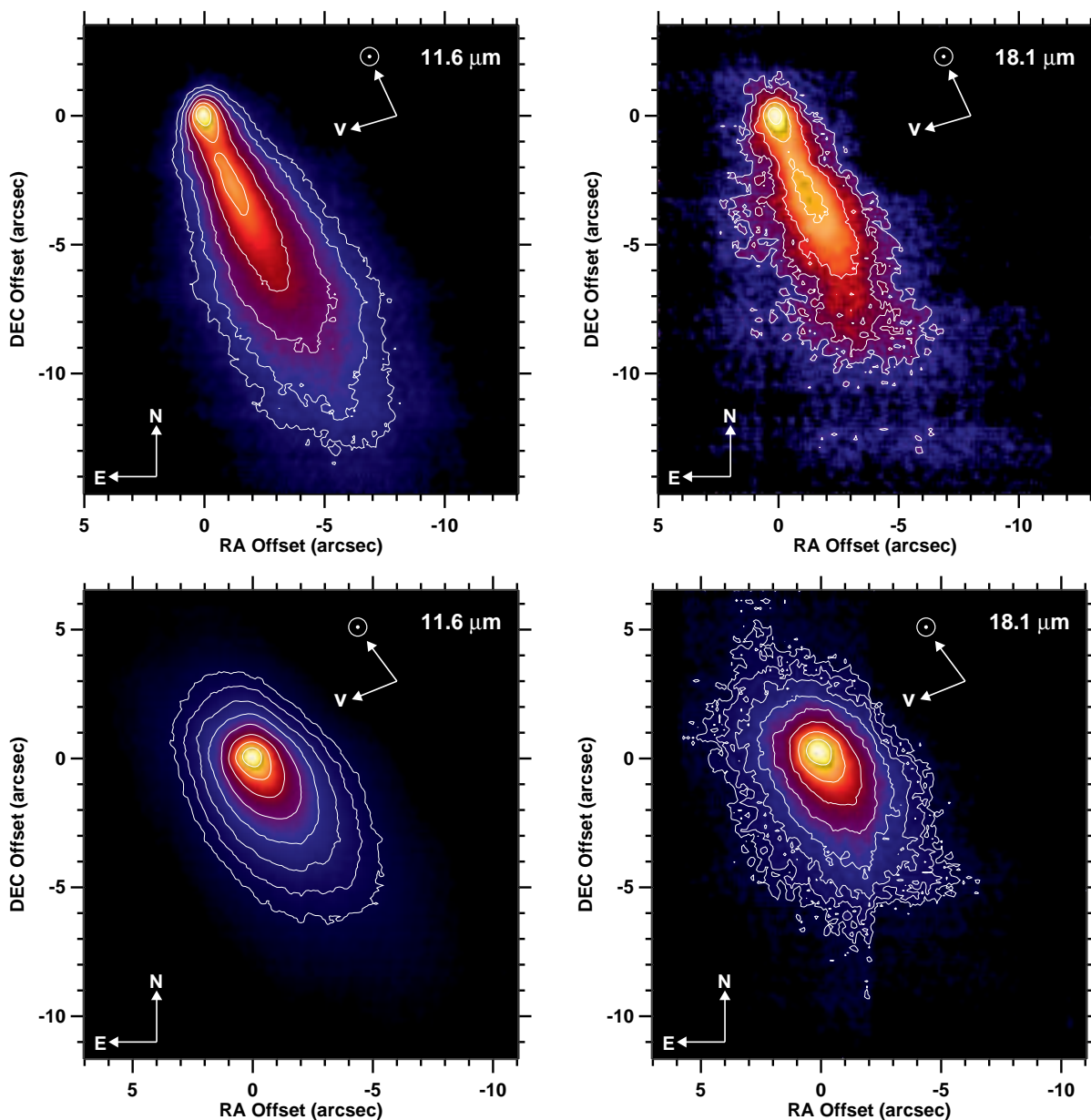


Fig. 1.— Images of comet 73P/Schwassmann-Wachmann 3 fragment SW3-[B] (*top row*) and fragment SW3-[C] (*bottom row*) at 11.6 μm (*left column*) and 18.1 μm (*right column*). The peak isophotes in the two panels for SW3-[B] represents 17.4 mJy, and for SW3-[C] represents 76.6 mJy. The ratio between isophotes in all panels is $\sqrt{2}$. The orientation of the frame on the sky, the direction of the Sun, and the direction of the velocity vector are indicated by arrows. The spatial scale of the panels for SW3-[B] is 1828×1828 km and for SW3-[C] is 1697×1697 km.

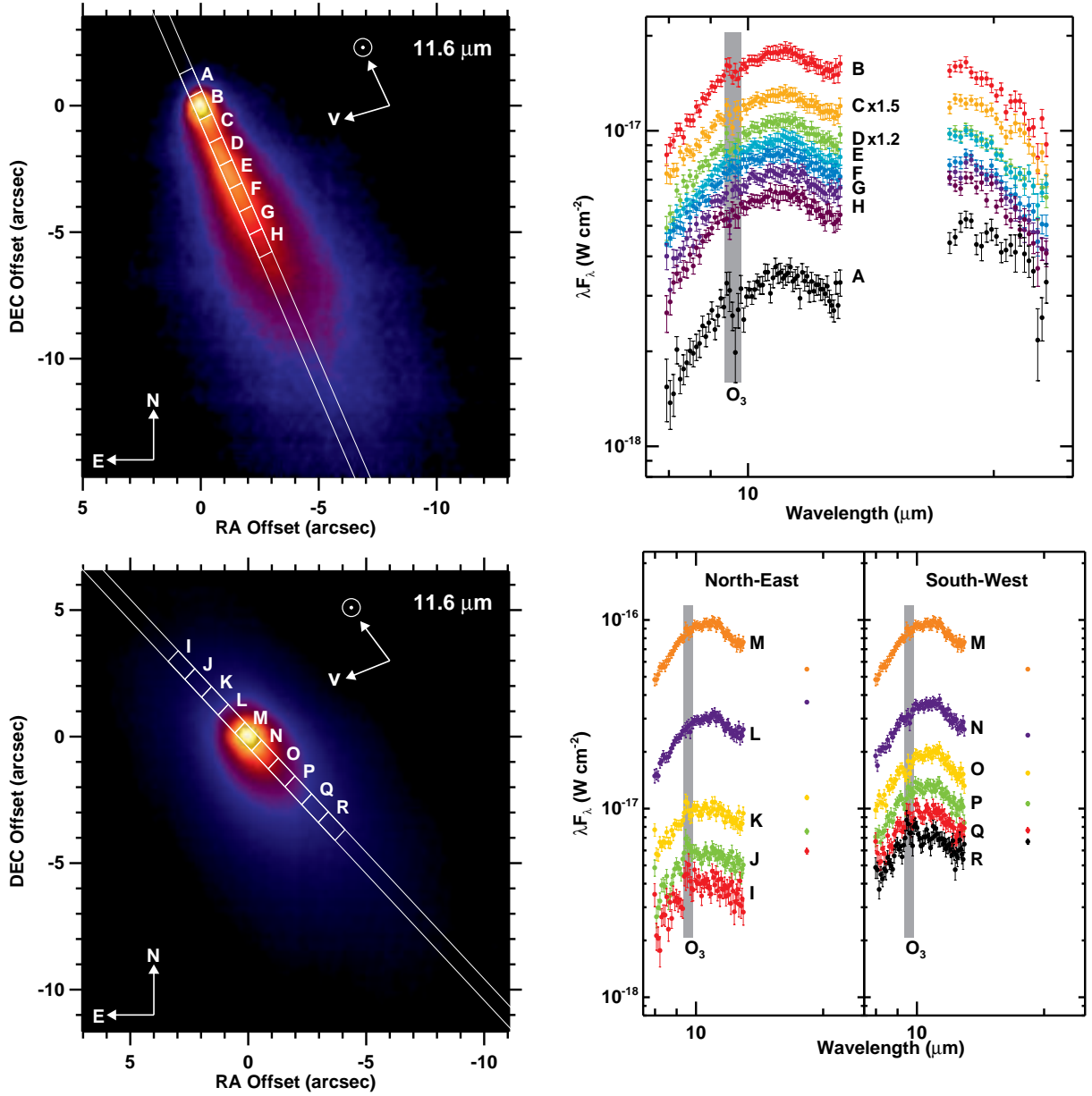


Fig. 2.— Spectral extractions of comet 73P/Schwassmann-Wachmann 3 fragments SW3-[B] (*top*) and SW3-[C] (*bottom*). The *left hand panels* are 11.6 μm images of the fragments which show the location of the slit and the size and location of the spectral extraction apertures (labeled with letters). The *right hand panels* show the 10 μm spectra for the fragments. For SW3-[B], the spectral extractions for locations C and D have been multiplied by a factor of 1.5 and 1.2, respectively, for display purposes. For SW3-[C], the extractions have been split to show extractions North-East of the nucleus (which is at extraction point M, and is shown on both sides for context) (*left*) and South-West of the nucleus (*right*). Also shown in the *right hand panels* are the 20 μm spectral extractions for fragment SW3-[B] and the 18.1 μm flux points for fragment SW3-[C].

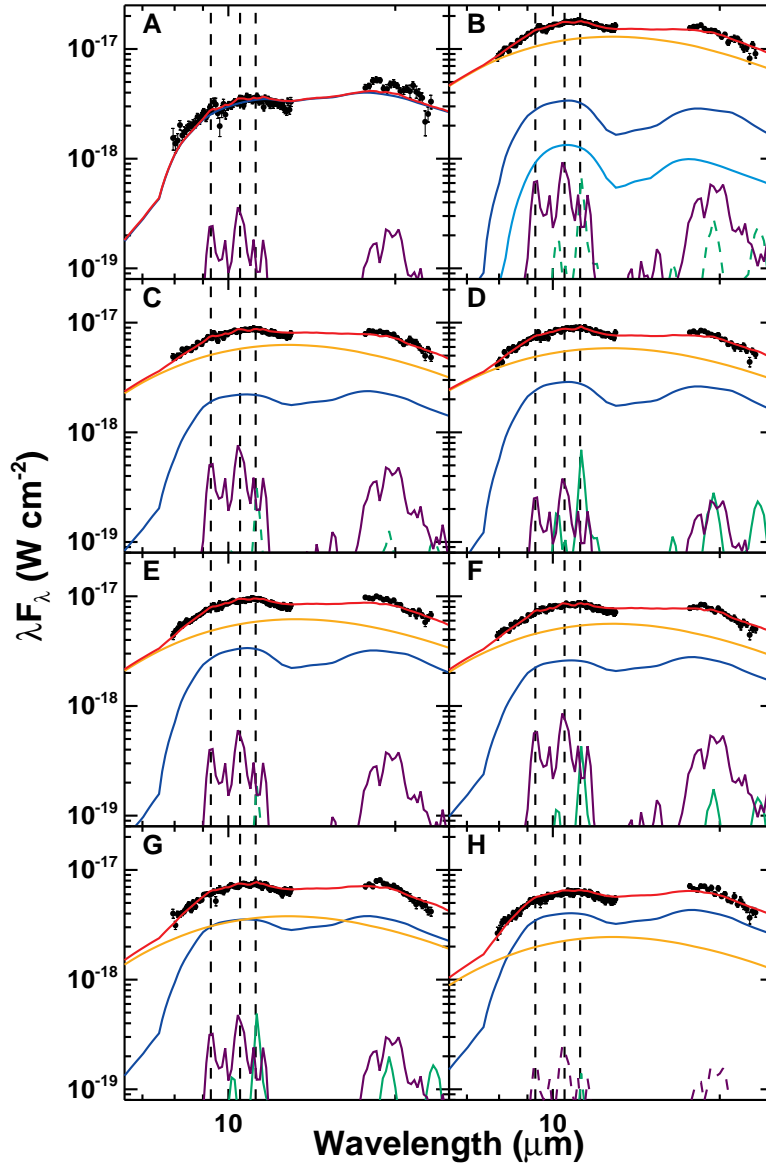


Fig. 3.— Spectral decomposition of model fits to the coma thermal spectra of comet 73P/Schwassmann-Wachmann 3 fragment SW3-[B]. The location of the extraction beam is indicated in each panel. Overlaid on the spectra (*black circles*) is the total SED fit (*red line*). The minerals used to create the SED are: amorphous pyroxene (*blue line*), amorphous olivine (*cyan line*), amorphous carbon (*orange line*), crystalline olivine (*green line*), and orthopyroxene (*violet line*). A solid line for a particular mineral indicates that the mineral is constrained by the model, a dashed line indicates that the mineral is not constrained. The three vertical *black dashed lines* indicate the wavelength locations for the resonance features of orthopyroxene at 9.3 and 10.5 μm and for crystalline olivine at 11.2 μm .

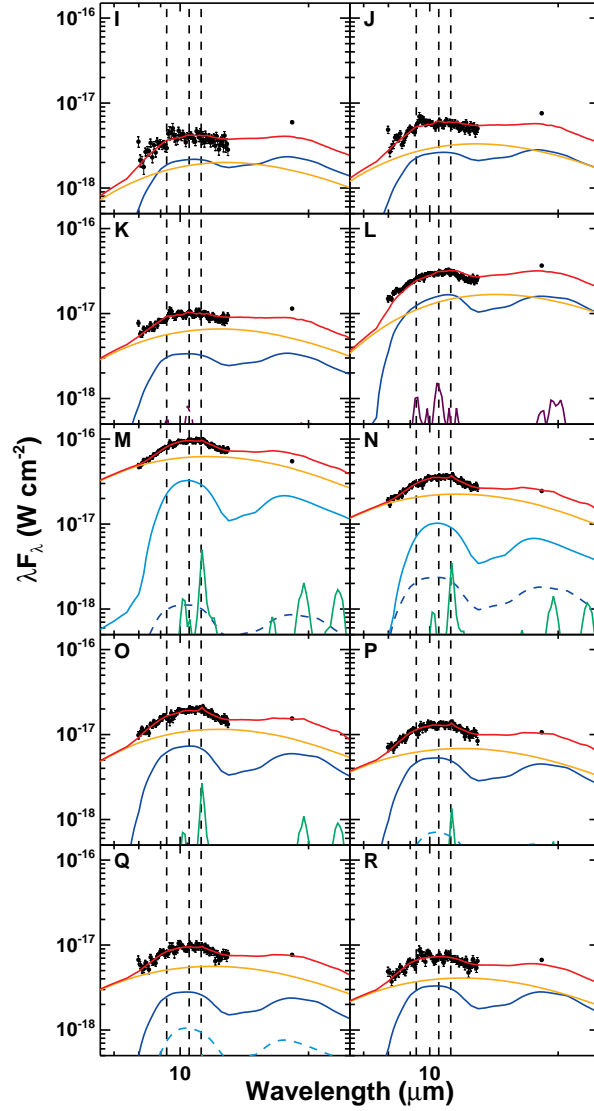


Fig. 4.— Spectral decomposition of model fits to the coma thermal spectra of comet 73P/Schwassmann-Wachmann 3 fragment SW3-[C]. The location of the extraction beam is indicated in each panel. Overlaid on the spectra (*black circles*) is the total SED fit (*red line*). The minerals used to create the SED are: amorphous pyroxene (*blue line*), amorphous olivine (*cyan line*), amorphous carbon (*orange line*), crystalline olivine (*green line*), and orthopyroxene (*violet line*). A solid line for a particular mineral indicates that the mineral is constrained by the model, a dashed line indicates that the mineral is not constrained. The three vertical *black dashed lines* indicate the wavelength locations for the resonance features of orthopyroxene at 9.3 and 10.5 μm and for crystalline olivine at 11.2 μm .

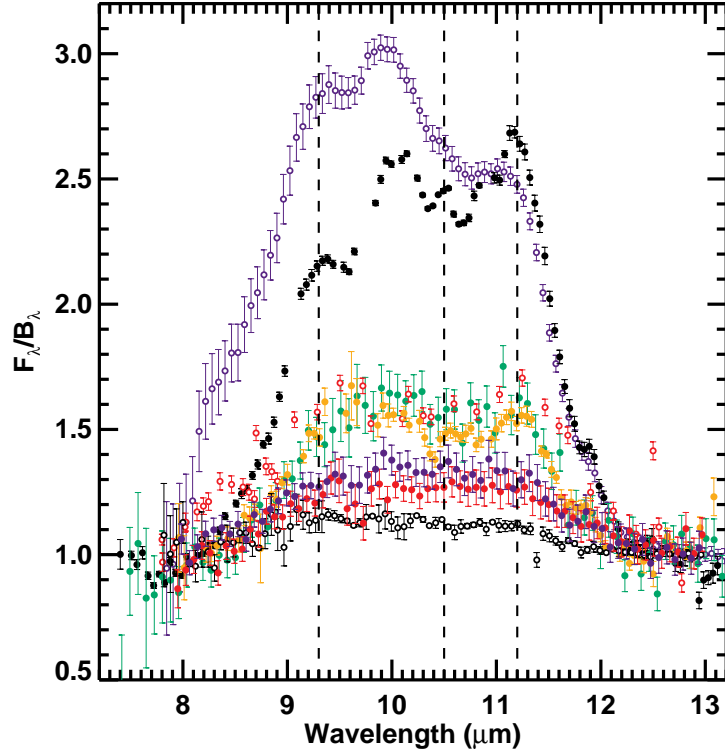


Fig. 5.— Blackbody normalized comet spectra extracted from slit positions coincident with each nucleus. The normalization is derived from fits to continuum spectral points $< 8.2 \mu\text{m}$ and $> 12.5 \mu\text{m}$ lying outside the silicate band. The blackbody normalized spectrum of comet 73P/Schwassmann-Wachmann 3 fragments SW3-[B] (*red*; $B_\lambda(T) = 289 \text{ K}$, $r_h = 1.11$, $\Delta = 0.15$) and SW3-[C] (*blue*; $B_\lambda(T) = 298 \text{ K}$, $r_h = 1.09$, $\Delta = 0.13$) $10 \mu\text{m}$ spectra are compared to other ecliptic (Jupiter family) and nearly isotropic (Oort cloud) comets observed with similar ground-based remote sensing techniques (except for C/2004 B1 (LINEAR) and 17P/Holmes which were observed with *Spitzer* and 1P/Halley which was observed with the Kupier Airborne Observatory): C/2004 B1 (Linear) (*open black circles*; $B_\lambda(T) = 215 \text{ K}$, $r_h = 2.06$, $\Delta = 1.60$), C/2001 Q4 (NEAT) (*orange*; $B_\lambda(T) = 310 \text{ K}$, $r_h = 0.97$, $\Delta = 0.35$), 9P/Tempel-1 post-Deep Impact (*green*; $B_\lambda(T) = 288 \text{ K}$, $r_h = 1.51$, $\Delta = 0.89$), 1P/Halley (*open red circles*; $B_\lambda(T) = 300 \text{ K}$, $r_h = 1.32$, $\Delta = 0.77$), C/1995 O1 (Hale-Bopp) (*black*; $B_\lambda(T) = 288 \text{ K}$, $r_h = 0.93$, $\Delta = 1.46$), and 17P/Holmes (*open blue circles*; $B_\lambda(T) = 206 \text{ K}$, $r_h = 2.51$, $\Delta = 1.87$) The *dashed lines* indicate the wavelengths of crystalline silicate emission features at 9.3 and $10.5 \mu\text{m}$ (orthopyroxene), and $11.2 \mu\text{m}$ (crystalline olivine).